

GLEAM: A Multimodal Imaging Dataset and HAMM for Glaucoma Classification

Jiao Wang, *Member, IEEE*, Chi Liu, Yiyang Zhang, Hongchen Luo, Zhifen Guo, Ying Hu, Ke Xu, Jing Zhou, Hongyan Xu, Ruiting Zhou, Man Tang

Abstract—Glaucoma is a leading cause of irreversible blindness worldwide, with asymptomatic early stages often delaying diagnosis and treatment. Early and accurate diagnosis requires integrating complementary information from multiple ocular imaging modalities. However, most existing studies rely on single- or dual-modality imaging, such as fundus and optical coherence tomography (OCT), for coarse binary classification, thereby restricting the exploitation of complementary information and hindering both early diagnosis and stage-specific treatment. To address these limitations, we propose glaucoma lesion evaluation and analysis with multimodal imaging (GLEAM), the first publicly available tri-modal glaucoma dataset comprising scanning laser ophthalmoscopy fundus images, circumpapillary OCT images, and visual field pattern deviation maps, annotated with four disease stages, enabling effective exploitation of multimodal complementary information and facilitating accurate diagnosis and treatment across disease stages. To effectively integrate cross-modal information, we propose hierarchical attentive masked modeling (HAMM) for multimodal glaucoma classification. Our framework employs hierarchical attentive encoders and light decoders to focus cross-modal representation learning on the encoder. The attention module, named multimodal-channel graph attention (MCGA), boosts glaucoma classification performance by emulating two key clinical reasoning steps: first, it uses a multi-head modality gating mechanism to replicate ophthalmologists' confidence scoring of fundus, OCT, and VF modalities; then, MCGA leverages a relational graph attention network to cross-examine structural-functional consistencies of weighted modalities. The experiments on GLEAM demonstrate that tri-modal fusion significantly outperforms single-modal and dual-modal configurations, and HAMM achieves superior performance compared with state-of-the-art multimodal learning methods. The dataset and code are publicly available via <https://kaggle.com/datasets/zhangyiyang/gleam-dataset>.

I. INTRODUCTION

Glaucoma is an irreversible, chronic ophthalmic disease and a leading cause of blindness worldwide. An estimated 70 million people are affected globally [1], and epidemiological

Manuscript received XX XX 2025. (Jiao Wang and Chi Liu are co-first authors.) (Corresponding author: Jiao Wang.)

Jiao Wang, Yiyang Zhang, Hongchen Luo, Zhifen Guo, Hongyan Xu, Ruiting Zhou, Man Tang are with College of the Information Science and Engineering, Northeastern University, Shenyang 110819, China (e-mail: wangjiao@ise.neu.edu.cn; 2470818@stu.neu.edu.cn; luohongchen@ise.neu.edu.cn; 2210301@stu.neu.edu.cn; 2400757@stu.neu.edu.cn; 2400990@stu.neu.edu.cn; 2470932@stu.neu.edu.cn).

Chi Liu, Ying Hu, Ke Xu, Jing Zhou are with the Department of Ophthalmology, Shenyang Fourth People's Hospital, Shenyang 110000, China (e-mail: huying.oculist@gmail.com; xuke830711@gmail.com).

projections suggest that by 2040, more than 110 million individuals will experience varying degrees of visual impairment due to the disease [2]. In clinical practice, diagnosis relies on a combination of imaging and functional assessments, including color fundus photography (CFP) for evaluating the optic nerve head, optical coherence tomography (OCT) for generating retinal nerve fiber layer (RNFL) thickness measurements to quantify structural thinning, and visual field (VF) testing for assessing functional deficits [3]–[5]. Accurate classification of glaucomatous visual field defects into different severity stages is clinically important, as it enables tailored treatment based on disease severity, facilitates more consistent follow-up, and provides a more reliable prognosis [6]. However, traditional manual diagnostic approaches suffer from several challenges, including slow processing speed, inconsistent accuracy, and a heavy reliance on physician expertise, underscoring the urgent need for more efficient and reliable diagnostic solutions.

To address these challenges, computer-aided diagnostic (CAD) systems have gained increasing attention. Over the past decade, numerous publicly available glaucoma datasets have been introduced focusing on a single modality [7]–[12]. Correspondingly, single-modal approaches [13]–[18] have been developed for glaucoma diagnosis, achieving steady improvements in accuracy and interpretability.

Despite these advances, single-modal systems are limited by the heterogeneous manifestations of glaucoma. Early lesions can be imperceptible in certain modalities, and modality-specific noise or artifacts further compromise reliability [19], [20]. Structure–function discordance is also common, where optic nerve changes may precede functional deficits or vice versa [21]. Clinical studies suggest that reliance on a single modality risks missing cases [22], [23]. These limitations motivate multimodal integration, as demonstrated by the GAMMA challenge [24] and subsequent multimodal fusion methods [25]–[29], which outperform single-modal approaches. Collectively, these findings highlight the clinical relevance and technical promise of multimodal analysis for glaucoma.

However, existing multimodal glaucoma datasets [24], [30]–[32] remain limited in scale, modality diversity, and staging granularity, hindering the exploitation of complementary information, early diagnosis, and stage-specific treatment. This inadequacy contrasts with clinical practice, where ophthalmologists routinely integrate fundus imaging for optic disc morphology, OCT-derived RNFL thickness for axonal integrity, and VF testing as the gold standard for functional loss. Each modality provides unique but incomplete information, and their

joint interpretation is critical for cross-validating suspicious findings, improving sensitivity to early or atypical cases, and mitigating errors caused by modality-specific artifacts or noise.

To overcome these limitations, we introduce **Glaucoma Lesion Evaluation and Analysis with Multimodal Imaging (GLEAM)** dataset, developed with Shenyang Fourth People's Hospital. As shown in Tab. I, GLEAM contains 1,200 samples, each with SLO fundus images, circumpapillary OCT images, and VF pattern deviation (PD) maps. All samples are annotated with a four-class glaucoma staging based on comprehensive clinical evaluation: non-glaucoma (NG), early glaucoma (EaG), intermediate glaucoma (InG), and advanced glaucoma (AdG). All modalities are acquired within a short temporal window to ensure cross-modality consistency. With its scale, modality coverage, and fine-grained staging, GLEAM provides a robust resource for developing and benchmarking fusion-based algorithms for glaucoma detection and staging.

In addition, to address the clinically critical challenge of integrating structural and functional imaging information, we propose the **hierarchical attentive masked modeling (HAMM)** framework for multimodal glaucoma classification. Diverging from conventional transformer-based masked autoencoders (MAE), HAMM is built entirely on convolutional neural networks (CNNs), which facilitates the integration of skip connections, a novel multimodal-channel graph attention (MCGA) module, and light decoders. The design of the MCGA module is clinically inspired; it emulates the ophthalmologist's practice [33], [34] of (i) assigning adaptive confidence weights to fundus, OCT, and VF modalities based on their quality and reliability, and (ii) cross-examining structural-functional consistencies. Specifically, MCGA employs a multi-head modality gating mechanism and a relational graph attention network that captures inter-modal dependencies. This architecture emphasizes robust representation learning within the encoder, thereby yielding richer and more transferable representations for downstream glaucoma classification tasks.

In conclusion, the main contributions of this paper include the following three aspects:

- We developed GLEAM, a novel multimodal glaucoma dataset that for the first time integrates tri-modal imaging with finer-grained stage annotations, supporting more precise and reliable research on glaucoma-aided diagnosis.
- We propose HAMM, which integrates a clinically inspired MCGA module and a designed MAE pretraining strategy to enable modality-aware fusion, achieving accurate and robust glaucoma classification.
- We compare HAMM with existing state-of-the-art (SOTA) models on GLEAM, demonstrating both the advantages of the tri-modal GLEAM dataset and the effectiveness of the proposed method.

The remainder of this paper is organized as follows: We review related work in Section II. In Section III, we propose our dataset. Section IV presents the details of the proposed method. In Section V, we report the experimental setup and results. Section VI provides a detailed discussion. Finally, we conclude this paper in Section VII.

II. RELATED WORK

A. Glaucoma Datasets

Over the past decade, several single-modality glaucoma datasets were released for glaucoma classification. Fundus-based datasets [7]–[11] supported optic disc/cup segmentation and fundus-based glaucoma detection. OCT dataset [12] mainly provided structural scans of the optic nerve head and RNFL for biomarker analysis. Specifically, Harvard Dataverse V1 (HDV1) dataset innovatively divided glaucoma into early and progressive stages, enabling the training of models with the capability to perform early-stage diagnosis, further advancing the potential for early intervention. While valuable, these single-modality datasets captured only partial aspects of glaucoma, motivating the development of multimodal datasets. The first small-scale multimodal glaucoma dataset, AFIO [30], was released in 2020 and contained only 50 samples, each comprising a fundus and an OCT image, labeled as either non-glaucoma or glaucoma. In 2021, the GAMMA dataset [24] was published with 200 samples and OCT/fundus modalities, which first stratified glaucoma into early and progressive stages in the multimodal domain, facilitating early diagnosis. The GRAPE dataset [31], published in 2023, addressed progression prediction by tracking patients over an average of 2.51 years. It classified 144 patients into progressive or non-progressive glaucoma based on longitudinal follow-up. Despite its longitudinal design, the cohort remained small. In 2024, the Harvard-GF dataset [32] expanded to 3,300 samples. It utilized OCT scans and derived RNFL maps for analysis. While larger, this dataset relies on two modalities derived from the same imaging source (OCT), limiting the upper limit of accuracy for multimodal classification. Other private datasets [35]–[38] (denoted as D1, D2, D3, and D4) exhibit similarly limited sample sizes and remain inaccessible to external researchers. More details are provided in Tab. I.

Existing datasets either suffer from small sample sizes, lack of accessibility, limited modality diversity, or staging granularity, which limits their utility for robust multimodal analysis. To address these gaps, we propose GLEAM, a novel public dataset comprising three image modalities and 1,200 clinical samples. This dataset introduces four categories: NG, EaG, InG, and AdG, representing the first multimodal glaucoma dataset to simultaneously offer the most image modalities and granular staging classification.

B. Glaucoma Classification Methods

Early glaucoma classification methods relied on a single modality, typically Fundus, OCT, or VF to train diagnostic models, achieving steady improvements in accuracy and interpretability through various architectures and longitudinal modeling [13]–[16]. Some methods [17], [18] use attention mechanisms to enhance glaucoma staging, achieving early diagnosis within a single modality. More recently, the focus has shifted towards multimodal fusion techniques [25], [26], [28], [38]–[41], where complementary information from different imaging sources is combined to achieve more accurate and robust glaucoma staging. Among these multimodal methods,

TABLE I: Overview of major glaucoma datasets for classification. (*NG*: Non-glaucoma, *EaG*: Early Glaucoma, *InG*: Intermediate Glaucoma, *AdG*: Advanced Glaucoma, *PG*: Progressive Glaucoma, *NPG*: Non-progressive Glaucoma.)

Dataset name	Year	Quantity	Imaging modalities	Classification	Public
ORIGA [7]	2010	650	Fundus	NG/G	✓
Drishti-GS [8]	2014	101	Fundus	NG/G	✓
Refuge [9]	2018	1200	Fundus	NG/G	✓
HDV1 [10]	2018	1542	Fundus	NG/EaG/PG	✓
ACRIMA [11]	2019	705	Fundus	NG/G	✓
Harvard-GDP [12]	2023	1000	RNFL	NG/G	✓
D1 [35]	2019	78	OCT & Fundus	NG/G	✗
AFIO [30]	2020	50	OCT & Fundus	NG/G	✓
GAMMA [24]	2021	200	OCT & Fundus	NG/EaG/PG	✓
D2 [36]	2022	1006	Fundus & RNFL	NG/G	✗
D3 [37]	2022	1110	OCT & OCTA	NPG/PG	✗
GRAPE [31]	2023	144	RNFL & VF	NPG/PG	✓
Harvard-GF [32]	2024	3300	OCT & RNFL	NG/G	✓
D4 [38]	2025	706	Fundus & RNFL & VF	NG/G	✗
GLEAM(Ours)	2025	1200	Fundus & OCT & VF	NG/EaG/InG/EdG	✓

attention-based techniques have emerged as a powerful approach to fuse information from different modalities. Attention mechanisms are particularly useful for capturing spatial and channel dependencies across modalities, enabling more accurate fusion and improving performance on complex tasks. MHCA [40] applies joint multi-head spatial-channel attention through 2D convolution and deconvolution operations with multiple kernel sizes, enhancing detail capture in low-resolution environments. However, this method incurs a high parameter count due to the repeated downsampling and upsampling operations. DRIFA-Net [41] incorporates robust residual attention and multimodal fusion attention in each convolution block, achieving hierarchical fusion, but at the cost of significantly higher parameters and computational time. To address these limitations, we propose the MCGA module, which integrates multimodal fusion more efficiently by incorporating an MCGA after each downsampling block in the CNN architecture. This design enables more effective hierarchical fusion. MCGA employs a multi-head modality-gating mechanism to assign adaptive confidence weights, and a relational graph attention network to capture inter-modal dependencies.

Furthermore, several studies [27], [29], [42]–[47] employ pre-training methodologies to enhance feature representation learning, subsequently fine-tuning models for classification tasks to improve glaucoma diagnostic accuracy. A prominent approach, supervised contrastive learning (SCL) [27], [29], [42], pulls embeddings from the same class closer together while pushing embeddings from different classes apart in the latent space, thereby maximizing inter-class discriminability. But unlike the classification with natural images, where the images with different labels are likely visually distinguishable, there is only a little difference in ophthalmology pictures with different labels [12]. This results in little to no role for the SCL method in the glaucoma classification task. Self-supervised learning (SSL), forcing models to learn contextual semantics without labels, offers an alternative pathway. MAE [43]–[47] is a representative SSL approach that learns contextual semantics through randomly masking image regions. Traditional MAE [43]–[46] is restricted to Transformer-based architectures, which lack visual inductive biases and rely heavily on large-scale annotated datasets. This makes MAE

prone to overfitting on small-sample medical datasets, where labeled data is limited and costly to obtain. Additionally, MAE suffers from high computational complexity and struggles to incorporate hierarchical feature learning, limiting its efficiency and performance. SparK [47] extended MAE to CNNs through a convolutional encoder-decoder, enabling hierarchical feature learning and achieving superior performance on downstream tasks. However, to the best of our knowledge, CNN-based MAE has not yet been applied to multimodal tasks. To address these limitations, we propose HAMM, which leverages CNN-based masked modeling with skip connections and the clinically inspired MCGA module, enabling adaptive weighting and cross-checking of multimodal data for more reliable and transferable representations.

III. GLAUCOMA DATASET

In this section, we introduce the GLEAM dataset. It comprises SLO fundus images, circumpapillary OCT images, and VF PD maps collected from a standardized clinical cohort with procedures for data acquisition, quality control, and image processing. This study is approved by the Institutional Review Board (IRB) of Shenyang Fourth People’s Hospital (Approval Number: 2025-ZFKY-021; Approval Date: 2025.09.08) and adheres to the Declaration of Helsinki. The IRB waives the requirement for informed consent due to its retrospective design. All unique patient identifiers are permanently deleted from the dataset to ensure the privacy and confidentiality of patients. GLEAM serves as a benchmark for developing multimodal staging models to improve glaucoma diagnosis and is publicly available under a CC BY-NC-ND 4.0 license.

A. Data Collection and Quality Control

As shown in Fig. 1 (a) and Fig. 1 (b), we retrospectively collect multimodal ophthalmic data from Shenyang Fourth People’s Hospital, China, including:

- **Scanning Laser Ophthalmoscopy (SLO) Images:** Acquired using the Optos ultra-widefield SLO device, providing high-resolution, wide-angle fundus imaging.
- **Circumpapillary Optical Coherence Tomography (OCT) Images:** Captured with the Heidelberg Spectralis OCT system, enabling detailed retinal layer analysis.

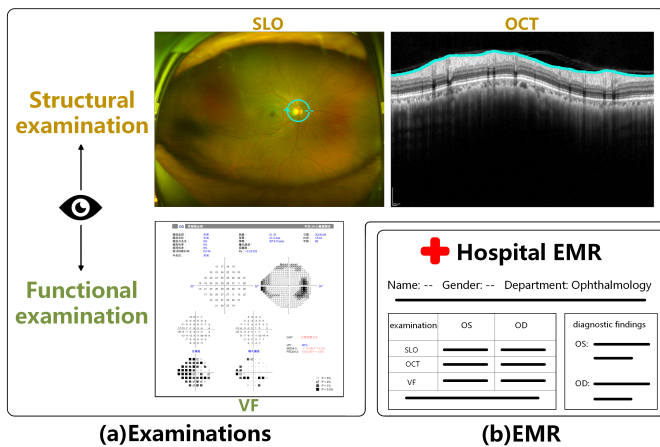


Fig. 1: The detail of ophthalmic data, including (a) SLO, OCT, and VF examinations (b) EMR documented by ophthalmologists.

- **Visual Field (VF) Reports:** Generated using Zeiss perimeter devices, with key metrics such as mean deviation (MD) and pattern standard deviation (PSD) recorded.
- **Electronic Medical Records (EMR):** Documented by ophthalmologists, including annotations of the patient details and ophthalmologists’ diagnostic findings.

To establish a robust dataset, rigorous quality control focused on diagnostic integrity and label consistency is implemented. We included only samples where the SLO and circumpapillary OCT images are clear, and both the false negative and false positive rates of VF are less than 33%. The labeling process consists of two stages: initial labeling and expert review.

In the initial labeling stage, four trained annotators evaluate comprehensive diagnostic findings for each potential participant, categorizing them into one of three groups: normal, presence of glaucoma-related findings, or other ophthalmopathies. To minimize confounding effects and isolate manifestations specific to glaucoma pathology, all samples designated as other ophthalmopathies are systematically excluded prior. Subsequently, retained samples are assigned to one of four categories: NG, EaG, InG, and AdG. This assignment integrates available diagnostic findings and quantitative metrics. Explicit diagnostic findings of disease stage within the EMR form the primary basis for label assignment. For samples lacking explicit stage specification, categorization relies on the MD value from VF reports using clinical stratification thresholds: early-stage ($MD > -6$ dB), intermediate-stage ($-12 \text{ dB} \geq MD \geq -6$ dB), and advanced-stage ($MD < -12$ dB). [48].

Following initial labeling, three senior ophthalmologists independently review all multimodal images and assign stage labels. This review (i) excludes samples with poor quality (e.g., defocus, low illumination, misalignment, or severe artifacts), and (ii) verifies label consistency with both image findings and clinical context. Any discrepancies are reconciled through expert consensus, thereby improving diagnostic accuracy and resolving ambiguities. To comprehensively assess the labeling quality, two types of consistency evaluations were performed. For inter-grader agreement, the pairwise consistency of the

TABLE II: Inter- and Intra-grader Agreement via Quadratic Weighted Cohen’s Kappa (%)

Agreement Type	Expert 1	Expert 2	Expert 3
Intra-grader Agreement	98.25	97.68	97.42
Expert 1 vs. Expert 2	95.81	-	-
Expert 1 vs. Expert 3	96.37	-	-
Expert 2 vs. Expert 3	-	95.59	-

first-round independent annotations from the three experts was calculated to reflect the consensus level among different clinicians. For intra-grader agreement, the three experts were asked to perform a second-round blind annotation on all retained samples after an interval of one month; it should be emphasized that this second-round annotation was conducted without access to their previous labeling records, and was used *solely for consistency verification rather than label modification—the formal labels used in all subsequent experiments were determined by the first-round annotations after expert consensus*. The quantitative results of both inter- and intra-grader consistency are summarized in Tab. II, where the quadratic weighted Cohen’s kappa coefficient was adopted to account for the ordinal nature of glaucoma staging.

B. Image Processing for Dataset

The processing pipeline mainly focuses on SLO images and VF reports, aiming to remove irrelevant information in the images. For SLO images, the optic disc centroid is manually adjusted to align with the image center across the dataset. A uniform region of interest (ROI) of 450×450 pixels is extracted, centered on the optic disc through a standardized cropping procedure. This ensures that the optic disc–cup region, the key area evaluated by ophthalmologists for glaucoma diagnosis [49], is consistently retained across samples, while peripheral retinal areas prone to distortion and vignetting in ultra-widefield imaging are removed.

For VF reports, an automated clipping procedure isolates the clinically critical Pattern Deviation map based on predefined coordinate boundaries relative to the report layout. The extracted 920×920 -pixel image retains numerical axes and labels. To prepare a clean image suitable for pixel-based analysis, these axes are removed by overwriting rectangular regions containing axis lines and tick marks with a constant white mask, retaining only the grayscale sensitivity value grid.

C. Dataset Character

The final dataset comprises 1,200 multimodal samples, each integrating VF PD maps, SLO fundus images, and circumpapillary OCT images. As shown in Fig. 2 (a), GLEAM dataset includes 600 NG, 200 EaG, 200 InG, and 200 AdG samples, corresponding to 841 Chinese patients (56% female). Patient ages ranged from 8 to 90 years (mean 55.4 ± 16.7 years). Of these, 482 patients provided data from both eyes, 249 patients provided oculus sinister (OS) data, and 233 patients provided oculus dexter (OD) data. This constitutes the first publicly available glaucoma dataset that simultaneously includes tri-modal imaging. The finer-grained four-classification system can also support more accurate diagnoses and treatments.

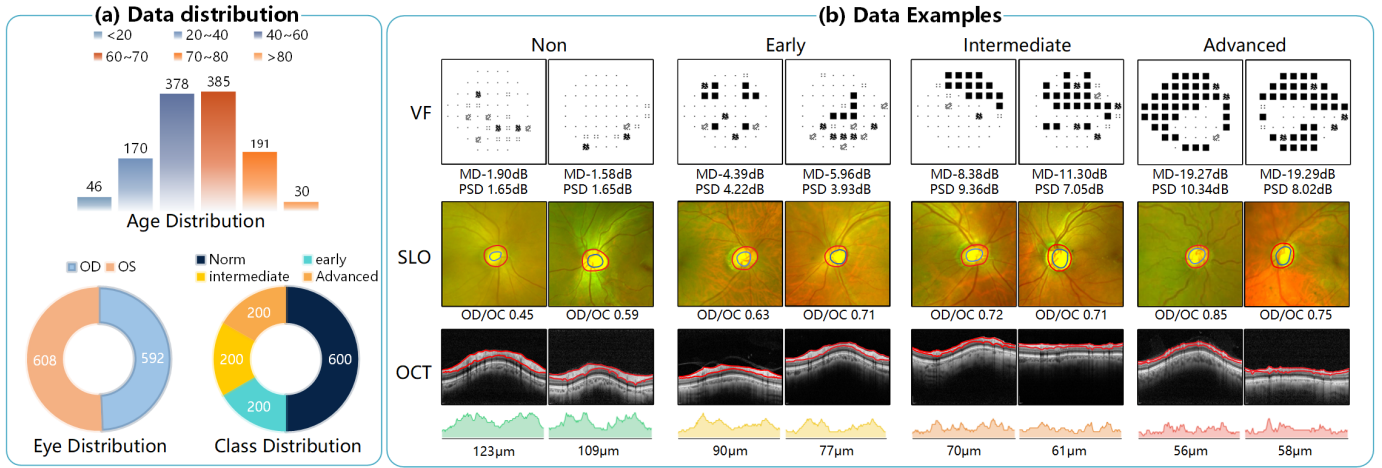


Fig. 2: GLEAM dataset character, including (a) distributions of GLEAM, and (b) examples of GLEAM. We add lines for splitting the optic disc/optic cup and the thickness of the RNFL to more visually show the gaps in the images of different progressions of glaucoma.

Fig. 2 (b) illustrates characteristic differences across glaucoma stages for each imaging modality. VF PD maps exhibit increasing numbers and spatial extent of dark patches, corresponding to progressive retinal ganglion cell dysfunction and declining visual sensitivity. Concurrently, SLO fundus images reveal progressive enlargement of the optic disc-to-cup (OD/OC) ratio, resulting from optic cup excavation due to axonal loss in the optic nerve head. Circumpapillary OCT images demonstrate progressive thinning, directly correlating with neural damage severity. Obviously, the visual field report is the easiest to distinguish among the EaG, InG, and AdG modalities, but its interpretation is subjective and depends on the patient’s degree of cooperation. Therefore, integrating complementary information from multiple modalities enables a more accurate assessment of glaucoma progression.

IV. PROPOSED METHOD

Fig. 3 shows the proposed HAMM. The inputs of HAMM are fundus images, circumpapillary OCT images, VF PD maps, and the corresponding labels represented as $\mathcal{D} = \{(\mathbf{X}_i, y_i)\}_{i=1}^N$, where $\mathbf{X}_i = \{X_i^f, X_i^o, X_i^v\}$ denotes the three image modalities of the i -th sample, y_i is its corresponding label, and N is the total number of samples. The target tasks are specifically addressed with $y_i \in \{0, 1, 2, 3\}$, corresponding to NG, EaG, InG, and AdG. During training, the inputs \mathbf{X}_i are used to generate enhanced multimodal representations $\mathbf{X}_i^S = \{S_i^f, S_i^o, S_i^v\}$. For validation and testing, $\mathbf{X}_i^S = \mathbf{X}_i = \{X_i^f, X_i^o, X_i^v\}$. The goal of our proposed method is to optimize parameters θ to learn a mapping function: $\mathcal{F}_\theta : \mathbf{X}_i \rightarrow p(y_i | \mathbf{X}_i)$, where $p(y_i | \mathbf{X}_i)$ is the class probability distribution. We utilize three ResNet-50 [50] as encoders represented as $\psi^f(\cdot), \psi^o(\cdot), \psi^v(\cdot)$. These encoders integrate MCGA modules at every layer to enhance feature representation through cross-modality dependency learning. The method then operates in two distinct stages: At stage one, we use a designed masked autoencoder architecture, enabling feature representation learning through reconstruction tasks. The masked inputs of three modalities represent as $\tilde{\mathbf{X}}_i^S$ are

encoded through $\psi^f(\cdot), \psi^o(\cdot), \psi^v(\cdot)$ to extract feature maps $\tilde{\mathbf{E}}_{1(i)}$. The feature maps then through our designed decoders $\phi^f(\cdot), \phi^o(\cdot), \phi^v(\cdot)$ to reconstruct the feature maps into $\mathbf{D}_{1(i)}$, minimized by MSE loss to approximate \mathbf{X}_i^S . At stage two, we employ the pre-trained backbone from stage one to extract feature maps $\mathbf{E}_{1(i)}$ from inputs \mathbf{X}_i^S and then classify by a classification head. Generally, the framework comprises three core components: (1) multimodal feature extraction with MCGA, (2) masked autoencoder pretraining for multimodal representation learning, and (3) fine-tuning for multimodal glaucoma classification.

A. Multimodal Feature Extraction with MCGA

We employ three parallel ResNet-50 networks as modality-specific encoders to extract hierarchical features from fundus images, OCT images, and VF PD maps. Each encoder consists of four sequential layers, progressively transforming input modalities into semantically enriched feature representations through dimensional reduction and receptive field expansion. For layer i , the modality-specific feature maps are computed as follows:

$$E_i^{k'} = \psi_i^k(E_{i-1}^k), \quad \mathbf{E}_i = \xi_i(\mathbf{E}_i'), \quad (1)$$

where $i = 1, 2, 3, 4$ indexes the layer, $k \in \{f, o, v\}$ denotes the modality, $\psi_i^k(\cdot)$ is the i -th layer of the k -th modality encoder, $\mathbf{E}_i' = \{E_i^{f'}, E_i^{o'}, E_i^{v'}\}$ is the collection of modality-specific features before attention refinement, $\xi_i(\cdot)$ is the MCGA module for multimodal-channel attention refinement, and $\mathbf{E}_i = \{E_i^f, E_i^o, E_i^v\}$ is the refined collection of modality-specific features after attention. Specifically, $\mathbf{E}_0 = \mathbf{X}^S$ denotes the collection of input images. The final outputs of the encoders are $\{E_4^f, E_4^o, E_4^v\}$.

For MCGA module, to capture complementary channel-wise information, each modality feature map $E^{k'}$ is summarized via global average pooling (GAP), global max pooling (GMP), and generalized mean (GeM) pooling as follows:

$$c^k = [GAP(E^{k'}) \parallel GMP(E^{k'}) \parallel GeM(E^{k'})], \quad (2)$$

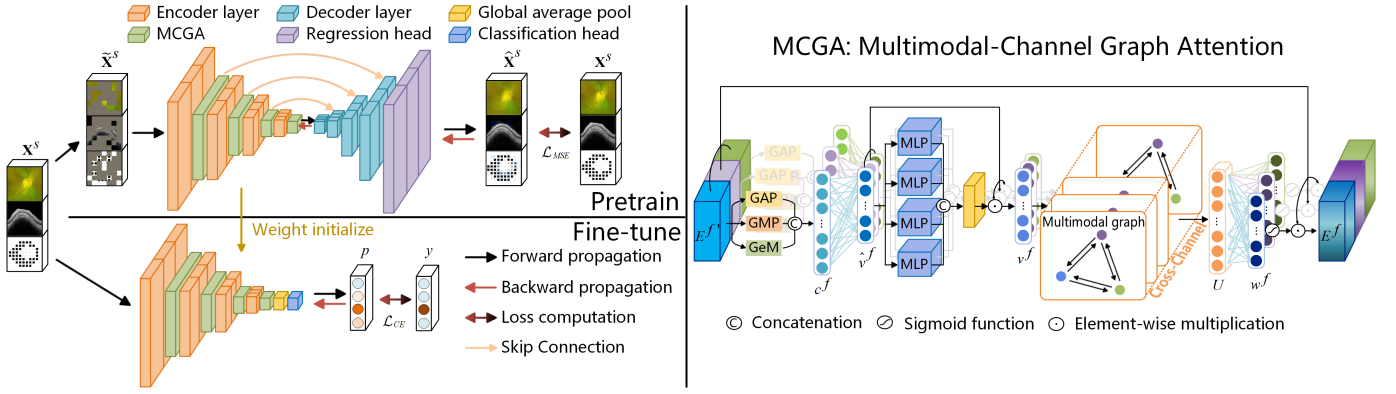


Fig. 3: The architecture of HAMM. Stage one is the masked autoencoder pretraining task to train a better feature representation, and stage two is the classification task to train the final classification model. The MCGA module is designed to model the multimodal information between different images when pretraining and classification. For clarity, token notations (e.g. c^f , \hat{v}^f , v^f) are shown for a single modality, though the same applies to all.

where C is the number of channels, and \parallel denotes vector concatenation. The concatenated pooled vector c^k is projected through a fully connected layer with sigmoid activation to generate the modality embedding as v^k , ensuring that the modality features are aligned in a way that facilitates the proper functioning of the subsequent graph convolutional attention mechanism.

Due to imaging artifacts, occlusions, or differences in modality-specific characteristics, each modality may exhibit varying degrees of uncertainty or quality. To account for the uncertainty inherent across multiple modalities, we introduce a multi-head, learnable gating mechanism that simulates the process of multiple ophthalmic experts assessing the reliability of each modality. By applying this gating mechanism, we aim to model the confidence or reliability of each modality's representation and incorporate this uncertainty into the attention mechanism, thereby improving the model's ability to selectively focus on the most informative features from each modality. The multi-head learnable gating mechanism is applied as follows:

$$\hat{v}^k = v^k \odot \frac{1}{H} \sum_{h=1}^H g^{(h)}(v^k), \quad (3)$$

where H is the number of heads, $g^{(h)}(\cdot)$ is the h -th gating function, and \odot denotes element-wise multiplication.

The gated embeddings from all modalities are stacked into a matrix $V = [\hat{v}^f, \hat{v}^o, \hat{v}^v] \in \mathbb{R}^{3 \times C}$. A relational graph attention mechanism is then applied to capture inter-modal dependencies. For each edge (i, j) with relation type r_{ij} and attention head h , the compatibility score is computed as:

$$e_{ij}^{(h)} = \text{LeakyReLU}\left(\left(a^{(h)}\right)^\top \left[W^{(h)} \hat{v}^i \parallel \left(W^{(h)} \hat{v}^j + R_{r_{ij}}^{(h)} \right) \right]\right), \quad (4)$$

where $W^{(h)} \in \mathbb{R}^{C \times C}$ is the per-head projection matrix, $R_{r_{ij}}^{(h)} \in \mathbb{R}^C$ is the embedding of relation type r_{ij} , $a^{(h)} \in \mathbb{R}^{2C}$ is the learnable attention vector. To obtain a proper weighting distribution, these raw scores are normalized across the neighbors of node i as follows:

$$\alpha_{ij}^{(h)} = \frac{\exp(e_{ij}^{(h)})}{\sum_{k \in \mathcal{N}(i)} \exp(e_{ik}^{(h)})}, \quad (5)$$

where $\mathcal{N}(i)$ denotes the set of neighbors of node i . The contextualized representation of node i is then aggregated from its neighbors across all heads as follows:

$$u^k = \frac{1}{H} \sum_{h=1}^H \sum_{j \in \mathcal{N}(i)} \alpha_{ij}^{(h)} (W^{(h)} \hat{v}^j + R_{r_{ij}}^{(h)}). \quad (6)$$

The updated embeddings from all modalities are stacked into a matrix $U = [u^f, u^o, u^v] \in \mathbb{R}^{3 \times C}$, which is subsequently passed through a fully connected layer with sigmoid activation to produce the final channel attention weights $\{w^f, w^o, w^v\}$.

Finally, the attention weights are applied to the original feature collection E^f to produce the refined feature:

$$E^k = E^{k'} \odot w^k, \quad (7)$$

where \odot denotes element-wise multiplication with broadcasting along the spatial dimensions.

B. Masked AutoEncoder Pretraining for Multimodal Representation Learning

In ophthalmic imaging, data can often be incomplete or compromised due to issues like ghosting, blurriness, and occlusions caused by anatomical structures. These are common across modalities such as fundus and OCT, making it difficult to capture high-quality images across all areas. To address these challenges, we incorporate a Masked AutoEncoder mechanism during the initial training phase. The MAE is particularly well-suited for ophthalmic images, which explicitly simulate missing or corrupted data by masking parts of the input image and training the model to reconstruct the occluded regions. This process encourages the model to learn robust, context-aware features that are less dependent on any single image region, thereby improving its ability to generalize to real-world scenarios where missing information or distortions are common.

For each modality k in the multimodal input X^S , we generate masked inputs using a structured masking approach:

$$\tilde{s}^k = s^k \odot M_k, \quad (8)$$

where M_k is a binary mask, $\|M_k\| = \rho \times \text{area}(x_{ki})$, and \odot denotes element-wise multiplication. The masked inputs $\tilde{X}^S = \{\tilde{s}^f, \tilde{s}^o, \tilde{s}^v\}$ are then fed into the encoder network to generate encoded feature maps $\{\tilde{E}_4^f, \tilde{E}_4^o, \tilde{E}_4^v\}$. By dynamically fusing the information across modalities in the encoder network, MCGA enables the model to focus on the most informative regions, compensating for missing or degraded parts in any single modality.

Subsequently, the encoded feature maps are passed through decoders $\phi_i^k(\cdot)$ to reconstruct the original images. Each decoder consists of four layers, where bilinear interpolation is used for up-sampling, followed by a depthwise separable convolution [51] to refine the feature maps. At each layer, the decoder takes as input both the output from the previous decoder layer and the corresponding encoder feature maps. To ensure compatibility, a convolutional layer $\delta_i^k(\cdot)$ projects the encoder features to the same spatial resolution and channel dimension as the decoder outputs, after which the two are fused via element-wise addition. The decoder block $\phi_i^k(\cdot)$ generates the output features as:

$$D_i^k = \phi_i^k(\delta_i^k(\tilde{E}_i^k) + D_{i+1}^k), \quad (9)$$

where $i = 4, 3, 2, 1$ indexes the layer, \tilde{E}_i^k denotes the projected encoder feature maps from the i -th layer, and D_{i+1}^k is the output from the previous decoder layer, with $D_5^k = \mathbf{0}$. The outputs of the decoders are $\{D_1^f, D_1^o, D_1^v\}$. We introduce a **regression head** to fulfill the image reconstruction task. Finally, we introduce a regression head to fulfill the image reconstruction task, where each modality-specific decoder output is passed through a separate convolutional layer to reconstruct the corresponding input image as follows:

$$\hat{S}_i^k = \rho^k(D_1^k), \quad (10)$$

where $\rho^k(\cdot)$ denotes the convolutional reconstruction head for modality k .

To train the model, we adopt the mean squared error (MSE) loss as the loss function, which can be calculated by:

$$\mathcal{L}_{MSE} = \frac{1}{N} \sum_{i=1}^N \sum_{k \in K} \sum_{p=1}^P (s_i^{k(p)} - \hat{s}_i^{k(p)})^2, \quad (11)$$

where N is the batch size, $K = \{f, o, v\}$ denotes the set of modalities, P is the number of masked pixels per image, $s_i^{k(p)}$ denotes the pixel intensity at position p in the original image, and $\hat{s}_i^{k(p)}$ represents the corresponding reconstructed pixel intensity. This reconstruction objective encourages the model to develop robust feature representations that preserve critical anatomical structures and pathological features despite significant input corruption.

C. Fine-tuning for Multimodal Glaucoma Classification

For the glaucoma classification downstream task, we perform fine-tuning on the pretrained model by discarding the decoder and retaining only the encoder for hierarchical feature

extraction. Given the inputs X_i^S , the encoder outputs three modality-specific feature maps $\{E_4^f, E_4^o, E_4^v\}$. For effective multimodal feature fusion, we utilize a simple but effective way [28], [52], concatenating the feature vectors from three feature maps into an enhanced feature map E_4 . Subsequently, a global average pooling layer is employed to convert the 2D feature map into a compact 1D feature vector as follows:

$$v_\alpha^k = \text{GAP}(E_4^k), \quad (12)$$

where, GAP denotes global average pooling layer, v_α^k denotes pooled feature maps. Finally, we employ two fully-connected layers with ReLU as the classification head to classify the feature vector into specific categories, and we denote the output possibility as a positive case for each input multimodal sample \mathbf{X} as p . We use Cross Entropy loss as the loss function. The Cross Entropy loss can be calculated by:

$$\mathcal{L}_{CE} = -\frac{1}{N} \sum_{i=1}^N \sum_{c=1}^C y_{ic} \log(p_{ic}), \quad (13)$$

where, N denotes the batch size, C denote the number of classes, i indexes the i -th sample in the batch, c indexes the class label, $y_{ic} \in \{0, 1\}$ is the true binary indicator, and $p_{ic} \in [0, 1]$ is the predicted probability that sample i belongs to class c , satisfying $\sum_{c=1}^C p_{ic} = 1$ for each sample i .

V. EXPERIMENTS AND RESULTS

A. Implementation details

1) *Experiment Environment*: All experiments are conducted in a Kaggle cloud environment utilizing an NVIDIA P100 GPU with 16 GB memory. During model training, we employ the Adam optimizer. A learning rate of 1×10^{-5} is used for pre-training models, while fine-tuning for the classification task utilizes a learning rate of 3×10^{-6} , yielding optimal performance across modalities. The dataset is split into training, validation, and test sets following a 6:2:2 ratio. Specifically, we adopt stratified random sampling to ensure that the class distribution in each subset matches that of the entire dataset, maintaining class balance across all partitions. The subsets are available in our publicly accessible dataset to guarantee the reproducibility of the experiments. For each modality, input images are resized to a resolution of 224×224 , and we apply the canonical per-channel pixel normalization with the parameters: mean = [0.485, 0.456, 0.406] and standard deviation = [0.229, 0.224, 0.225]. Our MCGA is configured with 4 attention heads.

During Stage 1, models are pre-trained for 20 epochs with a masking ratio of 0.7 and a batch size of 8. During Stage 2, we employ a batch size of 16 and perform validation after each training epoch. Training continues until the validation loss has plateaued for 10 consecutive epochs, triggering early stopping. To ensure statistical reliability, five independent training trials are conducted with random initialization, and the mean results across runs constitute the final performance scores.

2) *Data Augmentation*: To improve robustness and reduce overfitting, we apply data augmentation while training. SLO images undergo random resized crop, color jitter, and vertical flip; OCT images apply random color jitter; VF PD maps apply random vertical flip. Additionally, all three co-registered

TABLE III: Comparison of the results obtained by HAMM and several representative methods on the GLEAM dataset. Statistical significance of accuracy differences relative to the baseline method is evaluated using two-tailed paired t-tests. (*: $p < 0.05$; **: $p < 0.01$, where p denotes p -value. TL: Transfer Learning, SCL: Supervised Contrastive Learning, SSL: Self-supervised Learning.

Method	Pre-train	Acc	F1	AUROC	Kappa	Param	FLOPs
ResNet50 [50]	-	76.75±1.47	66.84±2.60	89.95±0.27	85.88±0.76	83.12	12.41
ResNet50 [50]	TL	77.67±0.86	70.19±0.93	92.14±1.81	87.00±0.55	83.12	12.41
ViT-S [54]	TL	77.75±1.52	69.62±3.79	91.79±0.48	88.03±0.64	65.21	12.75
ConvNeXt-T [55]	TL	79.00±0.76**	71.58±1.32	91.87±0.77	87.83±0.72	85.20	13.39
MHCA [40]	TL	78.16±0.63	69.97±3.20	92.28±0.27	87.14±0.75	248.29	17.63
DRIFA-Net [41]	TL	77.83±0.86*	69.70±1.96	92.42±0.10	86.75±0.57	931.31	88.48
Corolla [27]	SCL	78.67±0.74**	72.87±1.21	92.39±0.55	88.50±0.32	83.90	12.41
ETSCL [29]	SCL	79.08±0.80*	72.52±2.11	92.73±0.32	87.31±0.43	94.06	16.53
MultiMAE [45]	SSL	78.00±0.18*	69.02±2.18	90.64±0.26	86.98±0.37	86.83	50.42
UrFound [46]	SSL	78.67±0.35*	70.67±1.46	92.49±0.44	87.86±0.48	65.21	12.75
HAMM(ours)	SSL	81.08±0.63**	75.90±0.80	93.03±0.26	90.07±0.46	237.52	12.68

modalities share a synchronous horizontal flip to preserve anatomical consistency between left and right eyes. Flip operations are applied with 50% probability, and color jitter varies brightness, contrast, and saturation within [0.9, 1.1].

3) Evaluation metric: To evaluate the performance of the proposed model, we employ accuracy, F1-score, the area under the ROC (receiver operating characteristic) curve (AUROC), and Kappa as the evaluation metrics, where larger values indicate better performance. In addition, we use Expected Calibration Error [53] (ECE) and Brier score to analyze model reliability, where smaller values indicate better performance. ECE quantifies the discrepancy between predicted confidence and empirical accuracy across M probability bins as:

$$\text{ECE} = \sum_{m=1}^M \frac{|B_m|}{N} |\text{acc}(B_m) - \text{conf}(B_m)|, \quad (14)$$

where B_m denotes the m -th bin containing samples with predicted probabilities in the interval I_m , $|B_m|$ is the sample count in bin B_m , N is the total sample size, $\text{acc}(B_m)$ is the empirical accuracy in B_m , and $\text{conf}(B_m)$ is the average predicted confidence in B_m . The Brier score evaluates the mean squared deviation as:

$$\text{Brier} = \frac{1}{N} \sum_{i=1}^N \sum_{c=1}^C (p_{ic} - y_{ic})^2, \quad (15)$$

where $y_{ic} \in \{0, 1\}$ is the true binary indicator, and $p_{ic} \in [0, 1]$ is the predicted probability that sample i belongs to class c , satisfying $\sum_{c=1}^C p_{ic} = 1$ for each sample i , thereby providing complementary measures of uncertainty calibration beyond traditional classification metrics.

B. Comparison With SOTA Methods

To evaluate our method, we compare HAMM with several SOTA pre-trained approaches. We include commonly used backbones such as ResNet-50 [50], ViT-S [54], and ConvNeXt-T [55] with ImageNet-1K pre-trained weights, using the same approach as the baseline in [24]. Attention-based methods (MHCA [40], DRIFA-Net [41]), supervised contrastive learning methods (Corolla [27], ETSCL [29]), and self-supervised approaches (MultiMAE [45], UrFound [46]) are also compared.

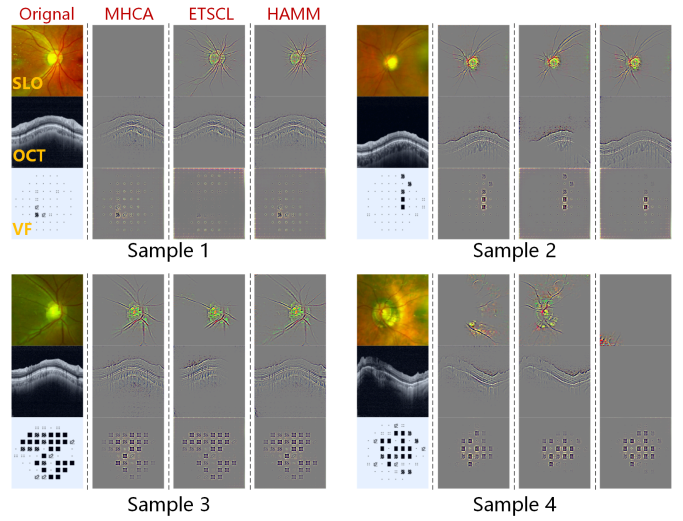


Fig. 4: Visualization of regions of interest identified by the model using Guided Grad-CAM.

As shown in Tab. III, HAMM achieves the best overall performance on the GLEAM dataset, with an accuracy of 80.75%, F1-score of 75.39%, and AUROC of 93.08%. For comparison, we next summarize the performance of representative methods. ResNet-50 performs better when using transfer learning method, with 1.00% increase in accuracy, 2.33% increase in F1-score, and 2.06% increase in AUROC. Among transfer learning models, ConvNeXt-T outperforms ViT-S and ResNet-50, but still falls short of HAMM, with 1.75% lower accuracy, 3.81% lower F1-Score, and 1.21% lower AUROC. Attention-based methods such as MHCA show improvement over ResNet-50, yet remain inferior to HAMM with 2.59% lower accuracy, 5.42% lower F1-score, and 0.8% lower AUROC. SCL approaches, such as ETSCL, enhance classification by pre-training to better distinguish inter-class features, but still perform slightly below HAMM with 1.67% lower accuracy, 2.87% lower F1-score, and 0.35% lower AUROC. SSL methods like MultiMAE achieves better performance than ViT through multimodal masked autoencoder, while UrFound utilizes knowledge-guided masked modeling to achieve competitive results. HAMM further employs a

TABLE IV: Experimental results of different modalities. Statistical significance of accuracy differences relative to the tri-modal method is evaluated using two-tailed paired t-tests. (*Acc-C_n*: accuracy for class *n*.)

Modality	Acc	F1	AUROC	Kappa	Acc-C1	Acc-C2	Acc-C3	Acc-C4
SLO	60.25**	37.25	74.72	56.79	94.83	3.00	2.00	72.00
OCT	61.75**	42.39	76.70	62.84	93.33	8.00	10.50	72.00
VF	74.25**	59.85	90.42	83.03	98.00	6.00	57.50	88.00
SLO+OCT	64.42**	46.47	67.22	79.72	94.00	11.00	13.50	80.00
SLO+VF	77.67*	68.36	91.87	86.84	96.33	26.00	61.50	89.50
OCT+VF	77.08*	67.38	92.24	86.25	96.50	22.50	61.00	89.50
SLO+OCT+VF	81.08	75.90	93.03	90.07	93.67	51.50	63.00	91.00

hierarchical attention module and light decoders to achieve superior integration of multimodal information, which yields the highest overall performance among all compared methods. In terms of parameter count, although HAMM has a relatively larger number of parameters than many methods, it is the most parameter-efficient attention-based method compared to others like MHCA and DRIFA-Net, both of which have significantly higher parameter counts. Additionally, HAMM performs impressively in terms of FLOPs, maintaining competitive computational efficiency despite the increase in model parameters.

Furthermore, we utilize guided gradient-weighted class activation maps [56] (Guided Grad-CAM) to show the focus areas of the model for the provided prediction in the input images. We choose three models (MHCA, ETSCl, and HAMM) and visualized several test samples from GLEAM to examine model attention as shown in Fig. 4. In the first sample (non-glaucoma), HAMM leverages ROI regions across all three modalities, while MHCA and ETSCl neglect SLO and VF images, respectively. In the second and third samples, Both MHCA and HAMM integrate lesion areas from VF PD, fundus, and OCT, outperforming ETSCl. For the last sample, HAMM primarily focuses on VF, reflecting the pronounced VF deviations that allow accurate classification. In comparison, while MHCA and ETSCl also exhibit a tendency to downweight SLO and OCT modalities and shift their focus toward VF, they suffer from incomplete attenuation of these two modalities. This distinction underscores the critical role of the MCGA module in HAMM for effective modality weight calculation.

C. Performance Analysis Across Modalities and Missing Modality

1) *Performance Analysis Across Modalities:* To comprehensively evaluate the impact of different modalities on classification accuracy, we conduct experiments with various modality combinations, as shown in Tab. IV. Among single modalities, VF provides the strongest discriminative ability, while dual-modal settings further enhance performance, particularly when VF is included. The tri-modal fusion achieves the highest performance and more balanced accuracy across classes, confirming the complementary benefits of integrating multimodality.

To further investigate the diagnostic value of multimodal fusion in glaucoma classification, we employ t-SNE dimensionality reduction to visualize feature representations extracted from optimally performing models under different modality combinations (VF, SLO+VF, and SLO+OCT+VF). As shown in Fig. 5 (a), the VF-only approach exhibits minimal inter-class

separation between adjacent disease stages. Notably, substantial overlap persists between intermediate and advanced stage samples. In Fig. 5 (b), the dual-modality approach demonstrates a significant enhancement of class separation. The margin between early and intermediate stages widens considerably, and overlap between intermediate and advanced groups is markedly reduced. As shown in Fig. 5 (c), the tri-modality approach demonstrates optimal separation performance with maximized inter-class margins across all disease stages, and refines discrimination between early and intermediate stage cohorts. Complementing the feature visualization results, the confusion matrices in Fig. 5 (e), (f), and (g) further quantify the classification robustness of the three modality combinations in clinical diagnosis scenarios. Specifically, the VF-only model in Fig. 5 (e) nearly loses the capability of early-stage glaucoma diagnosis, indicating its limited practical utility for timely intervention. For the dual-modality model depicted in Fig. 5 (f), the diagnostic performance is improved compared with the VF-only setting, yet non-negligible misclassification phenomena remain: NG cases are incorrectly categorized as AdG, and AdG cases are misidentified as NG. By contrast, the tri-modality model in Fig. 5 (g) achieves the most substantial improvement in diagnostic accuracy; the aforementioned cross-misclassification issues between NG and AdG are completely eliminated, which verifies the advantages of integrating multimodality.

2) *Performance Under Missing Modality Scenarios:* In practice, not all patients undergo complete examinations, and certain modalities may be unavailable due to factors such as equipment limitations or patient non-compliance. To simulate these realistic scenarios, we design an experiment where missing modalities are introduced during both training and evaluation.

During training, for each sample of each training epoch, we randomly remove one modality with a probability of 25%, two modalities with a probability of 25%, and keep all modalities intact with a probability of 50%. As a result, the same sample may have different missing modalities across epochs, helping expose the model to a variety of missing-modality scenarios. For the validation and test sets, we retain the original full-modality samples, then add new samples by modifying 50% of the original samples to have one modality missing, and 50% to have two modalities missing. In these modified sets, the distribution of missing modalities is consistent, with equal numbers of samples having each modality missing. This results in the test set having 480 samples (240 full-modality, 120 with one modality missing, and 120 with two modalities missing), and similarly, the validation set also grows to 480

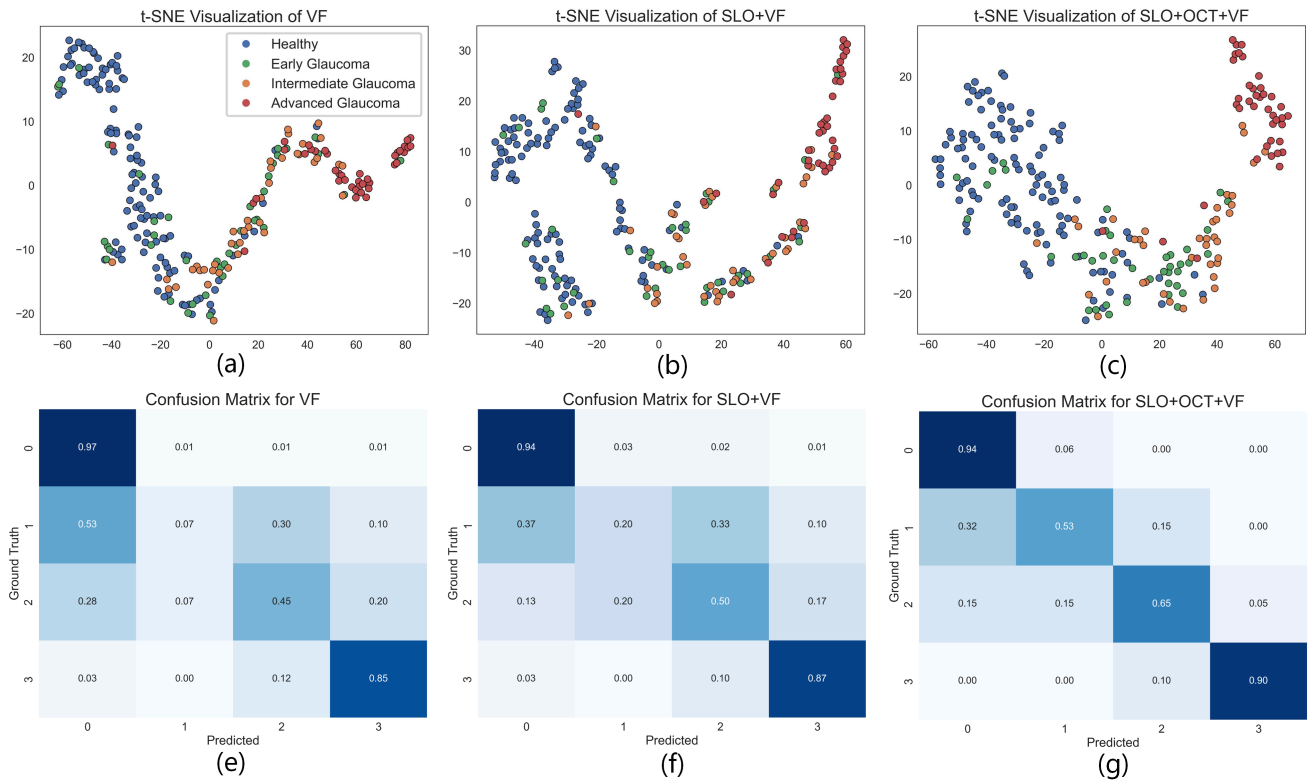


Fig. 5: Comprehensive evaluation of model feature representations and classification performance under three input settings: (a), (b), and (c) are t-SNE visualizations of feature embeddings corresponding to the input settings of VF, SLO+VF, and SLO+OCT+VF respectively; (e), (f), and (g) are confusion matrices corresponding to the identical set of input combinations.

TABLE V: Model performance under missing-modality scenarios.

Modality	Acc	F1	AUROC	Kappa
Corolla	69.87	60.42	84.65	73.15
ETSCL	70.35	61.76	84.89	73.22
MultiMAE	71.62	64.15	85.76	75.25
URFound	72.48	64.89	86.83	76.28
HAMM(Ours)	74.59	66.73	88.92	77.05

samples after applying the missing-modality configurations. The subsets of missing modalities used for validation and testing are available in our publicly accessible dataset to guarantee the reproducibility of the experiments.

Tab. V shows the performance of the model under different missing-modality conditions. As expected, the model's accuracy declines when one or more modalities are missing. However, even when faced with missing modalities, the model performs reasonably well, demonstrating the effectiveness of multimodal fusion and the model's ability to adapt to incomplete input. Models trained with randomly missing modalities during fine-tuning show greater robustness in handling missing data compared to those trained without such variation.

D. Reliability Analysis

We further evaluate model calibration using reliability diagrams. As shown in Fig. 6(a), tri-modal fusion consistently

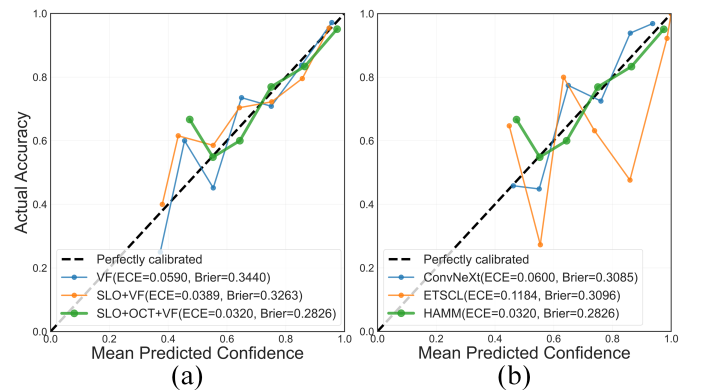


Fig. 6: Reliability diagram of models, including: (a) reliability diagram for different modalities VF, SLO+VF, and SLO+OCT+VF, and (b) reliability diagram for SOTA methods ConvNeXt, ETSCl, and HAMM.

achieves better calibration than single- and dual-modal settings, showing the most reliable confidence estimates. Fig. 6(b) compares the best three methods (ConvNeXt, ETSCl, and HAMM), where ETSCl exhibits poor calibration despite high accuracy, ConvNeXt trades slight reliability for performance, and HAMM achieves both high accuracy and well-calibrated predictions. These results demonstrate that accuracy and reliability do not always coincide. However, our proposed HAMM effectively enhances both through pre-training and

TABLE VI: The ablation study results of HAMM.

MCGA	Pre-train	Acc	F1	AUROC	Kappa
		77.67	70.19	92.14	87.00
✓		79.17	71.93	92.89	89.52
	✓	79.67	73.68	92.83	89.57
✓	✓	81.08	75.90	93.03	90.07

attention mechanisms. Notably, unlike single-modality and dual-modality, the tri-modality reliability curve lacked segments near the 0.4 confidence level, which indicates the model assigned consistently higher confidence scores, consequently resulting in no samples falling within this range. These results demonstrate that multimodal fusion not only enhances accuracy but also improves confidence calibration, showing better reliability.

E. Ablation Analysis

1) *Component Ablation*: Ablation studies are conducted to disentangle the contributions of the MCGA module and the MAE mechanism. As shown in Tab. VI, both components independently enhance model performance across multiple metrics. MCGA shows relatively stronger improvements in AUROC, indicating its role in refining discriminative feature representations and reducing irrelevant activations. Our MAE provides more noticeable gains in accuracy and F1-Score, suggesting improved robustness and generalization through representation learning. When integrated, the two modules complement each other and deliver the best overall performance, highlighting their synergistic effect.

2) *Effect of MCGA*: To further investigate the contribution of each component in the MCGA module, we evaluate its individual components in detail. For the pooling scheme, we compare our proposed approach with the commonly used GAP. For the attention scheme, in addition to ablating the two key components of MCGA, we also compare our attention mechanism with CBAM [57], a widely adopted attention mechanism that applies both channel and spatial attention to refine feature representations. In our multimodal setup, we first concatenate the different modalities along the channel dimension, then pass the concatenated features through the CBAM attention mechanism. Finally, a convolutional projection layer maps the attention-enhanced features back to the individual modalities. Furthermore, we examine two fusion strategies: late fusion, which applies fusion attention after encoding all modalities, and hierarchical fusion, which performs fusion at each convolutional layer, allowing for more localized and progressive feature aggregation. As shown in Fig. VII, the results of the ablation study confirm the effectiveness of the individual components in the MCGA module. Notably, when applying hierarchical fusion, while the parameter count increases significantly due to the additional attention mechanisms at each layer, the increase in FLOPs is minimal. This shows that our method achieves improved performance without a substantial computational cost. The combination of the full MCGA module in hierarchical fusion yields the highest performance across all metrics, further emphasizing its efficacy in enhancing multimodal fusion and feature representation.

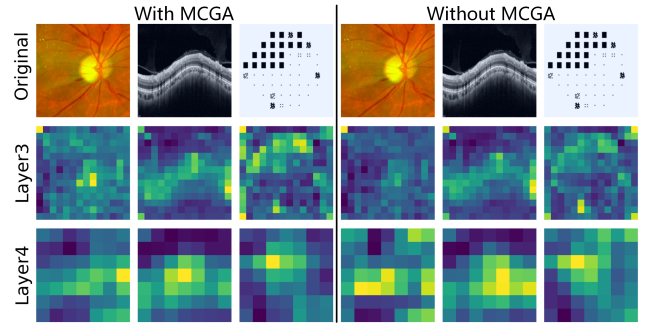


Fig. 7: Visualization of averaged feature maps from the 3rd and 4th backbone layers with and without the MCGA module.

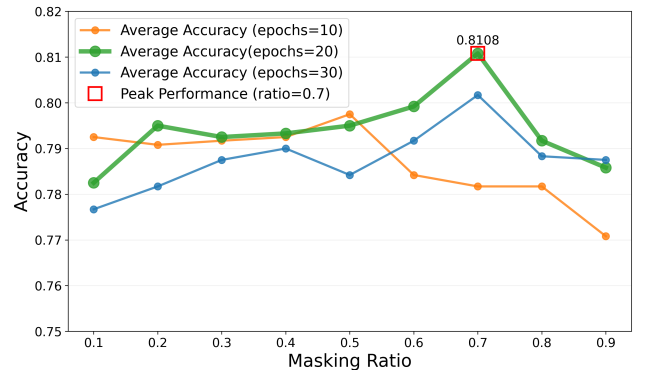


Fig. 8: Impact of masking ratio on model accuracy, with the optimum at 0.7 when trained for 20 epochs.

We also visualize the averaged feature maps from the 3rd and 4th layers of the backbone with and without MCGA. As shown in Fig. 7, feature responses become more concentrated on informative multimodal regions when MCGA is applied, indicating that MCGA effectively enhances feature representation.

3) *Masking Ratio Optimization Analysis*: To investigate the impact of masking ratio, we conduct experiments with ratios ranging from 0.1 to 0.9. As shown in Fig. 8, the model accuracy increases steadily, peaking at 80.75% with a masking ratio of 0.7 after 20 epochs of training, while further increase in the ratio leads to a noticeable decline. These results suggest that a moderate masking ratio, coupled with sufficient training, encourages the model to learn more discriminative features. Therefore, a masking ratio of 0.7 is identified as the optimal parameter configuration under the 20-epoch training setting for this task.

F. External validation on the GAMMA dataset

We added an external validation experiment using the GAMMA dataset [24]. GAMMA is a multimodal glaucoma classification dataset comprising paired 2D CFP images and 3D OCT volumes. As the official evaluation server of GAMMA only reports quadratically weighted Cohen’s Kappa, we follow this standard metric for all comparisons.

Since HAMM is designed to process multiple 2D image modalities, we converted the 3D OCT volumes into 2D RNFL thickness maps using the same preprocessing strategy as

TABLE VII: Ablation study results showing the contribution of different components in the MCGA module.

Pooling Scheme	Attention Scheme	Fusion Scheme	Acc	F1	AUROC	Kappa	Param	FLOPs
-	CBAM [57]	Late	78.00	70.89	92.14	87.93	125.59	14.27
-	CBAM [57]	Hierarchical	78.62	71.46	92.51	88.42	139.53	19.83
GAP only	Gating only	Hierarchical	77.75	70.61	92.49	87.02	131.68	12.49
GAP only	Graph only	Hierarchical	78.59	71.15	92.41	87.92	166.70	12.60
GAP only	Full Attention	Hierarchical	78.75	71.82	92.66	88.76	233.55	12.66
Full Pooling	Full Attention	Late	78.50	71.25	92.36	88.30	118.80	12.46
Full Pooling	Full Attention	Hierarchical	79.17	71.93	92.89	89.52	237.52	12.68

TABLE VIII: Comparison of Quadratic Weighted Kappa Results Between HAMM and SOTA Methods on the GAMMA dataset. (Add Info.: Use additional ophthalmic data for training, Add Mod.: Use additional modality)

Method	Add Info.	Add Mod.	Ensemble	Kappa
SamrtDSP [24]	✗	✗	✓	85.49
COROLLA [27]	✗	✗	✓	85.50
ETSCL [29]	✗	✓	✗	88.44
Mstnet (ResNet50) [26]	✓	✗	✗	86.00
GeCoM-Net [28]	✗	✗	✗	86.00
GeCoM-Net [28]	✗	✗	✓	88.10
Ours (HAMM)	✗	✗	✗	87.59
Ours (HAMM)	✗	✗	✓	89.35

COROLLA [27]. We applied the same data augmentation operations as COROLLA during training to maintain consistency with prior work on this benchmark.

The results on GAMMA are summarized in Tab. VIII, where HAMM is compared with several recent SOTA methods. Given that many comparative methods reported performance using ensemble strategies, we not only provide the standalone performance of our single model but also supplement it with an ensemble result for fair benchmarking. For the ensemble implementation, we select the three models with the highest kappa values and compute the mean of their predictions. Furthermore, ETSCL [29] employs an additional modality branch, while Mstnet [26] utilizes additional ophthalmic data for training. These two key characteristics have been explicitly indicated in the table. The results demonstrate that HAMM maintains competitive performance on this external dataset, suggesting robustness and generalizability across datasets with different acquisition protocols and modalities.

VI. DISCUSSION

HAMM demonstrates significant advantages in glaucoma classification by effectively integrating multiple imaging modalities—SLO, OCT, and VF testing. By leveraging hierarchical attention mechanisms, HAMM not only learns robust multimodal feature representations but also emulates clinical reasoning by assigning adaptive weights to each modality. This enables the model to capture the interplay between structural and functional data, improving the overall classification performance. The results show that HAMM outperforms single-modality and

traditional dual-modality approaches, making it a promising tool for accurate glaucoma diagnosis and staging.

In clinical practice, the accurate assessment of glaucoma progression relies heavily on both structural and functional information. While our model integrates multimodal imaging, we recognize that VF data may not always be available or feasible for every patient. Therefore, to enhance clinical translation, we plan to explore the model’s performance when VF data is excluded or when the model is trained with stratified MD bins. Additionally, to align better with clinical staging, we are considering the introduction of an ordinal loss function in future versions of our model. This would provide a more clinically intuitive representation of glaucoma progression, where each stage reflects a meaningful transition in disease severity.

Despite the promising results, there is one limitation to our study: the generalizability of the model. The current dataset is collected from a single clinical center using specific imaging devices. To improve the model’s robustness and ensure its applicability across different clinical environments, future work will include multi-center data validation and the exploration of domain adaptation methods.

An important consideration in glaucoma diagnosis is the heterogeneity of disease subtypes. Different subtypes, such as primary open-angle glaucoma, normal-tension glaucoma, pseudoexfoliative glaucoma, and angle-closure glaucoma, have distinct pathophysiological features and spatial patterns of damage. Currently, our dataset does not account for these variations, which could potentially affect the model’s learning process. Future research should include explicit labeling of glaucoma subtypes or employ domain adaptation techniques to better address the subtype-specific variations. Incorporating this information will improve the model’s ability to differentiate between the nuances of various glaucoma subtypes and enhance its clinical applicability.

VII. CONCLUSION

In this paper, we introduced GLEAM, the first publicly available tri-modal glaucoma dataset, and proposed HAMM, a novel multimodal fusion network designed to effectively capture inter-modal dependencies and enhance feature robustness through the MCGA module and masked modeling. Comprehensive evaluations demonstrate that tri-modal fusion consistently yields superior diagnostic accuracy and reliability compared with single-modal or dual-modal approaches. HAMM also surpasses

a range of SOTA methods, while maintaining well-calibrated predictions.

Beyond improving automated glaucoma detection, our work provides the community with a tri-modal dataset and open-source implementation, supporting exploration of intrinsic relationships among modalities to uncover underlying physiological mechanisms of glaucoma. By facilitating a deeper understanding of disease progression, this dataset contributes to early diagnosis and ultimately promotes public eye health. Future research may explore domain adaptation, semi-supervised learning, longitudinal analysis, and missing modality problem to further enhance diagnostic performance and generalizability.

REFERENCES

- [1] T. Vos *et al.*, “Global, regional, and national incidence, prevalence, and years lived with disability for 310 diseases and injuries, 1990–2015: a systematic analysis for the global burden of disease study 2015,” *The Lancet*, vol. 388, no. 10053, p. 1545–1602, 2016.
- [2] Y.-C. Tham *et al.*, “Global prevalence of glaucoma and projections of glaucoma burden through 2040: A systematic review and meta-analysis,” *Ophthalmology*, vol. 121, no. 11, pp. 2081–2090, 2014.
- [3] S. Choe *et al.*, “Natural history of optic disc with physiologic large cup: Incidence, predictors of glaucoma conversion after minimum 10-year follow-up,” *American Journal of Ophthalmology*, vol. 254, pp. 150–160, 2023.
- [4] M. Yu *et al.*, “Risk of visual field progression in glaucoma patients with progressive retinal nerve fiber layer thinning: A 5-year prospective study,” *Ophthalmology*, vol. 123, no. 6, pp. 1201–1210, 2016.
- [5] S. Asano *et al.*, “Early detection of glaucomatous visual field progression using pointwise linear regression with binomial test in the central 10 degrees,” *American Journal of Ophthalmology*, vol. 199, pp. 140–149, 2019.
- [6] P. Brusini and C. A. Johnson, “Staging functional damage in glaucoma: Review of different classification methods,” *Survey of Ophthalmology*, vol. 52, no. 2, pp. 156–179, 2007.
- [7] Z. Zhang *et al.*, “Origa-light: An online retinal fundus image database for glaucoma analysis and research,” in *2010 Annual International Conference of the IEEE Engineering in Medicine and Biology*, 2010, pp. 3065–3068.
- [8] J. Sivaswamy *et al.*, “Drishti-gs: Retinal image dataset for optic nerve head(ONH) segmentation,” in *2014 IEEE 11th International Symposium on Biomedical Imaging (ISBI)*, 2014, pp. 53–56.
- [9] J. I. Orlando *et al.*, “Refuge challenge: A unified framework for evaluating automated methods for glaucoma assessment from fundus photographs,” *Medical Image Analysis*, vol. 59, p. 101570, 2020.
- [10] J. M. Ahn *et al.*, “A deep learning model for the detection of both advanced and early glaucoma using fundus photography,” *PLoS ONE*, vol. 13, 2018.
- [11] A. Diaz-Pinto *et al.*, “Cnns for automatic glaucoma assessment using fundus images: an extensive validation,” *BioMedical Engineering OnLine*, vol. 18, 2019.
- [12] Y. Luo *et al.*, “Harvard glaucoma detection and progression: A multimodal multitask dataset and generalization-reinforced semi-supervised learning,” in *2023 IEEE/CVF International Conference on Computer Vision (ICCV)*, 2023, pp. 20414–20425.
- [13] H. Fu *et al.*, “Disc-aware ensemble network for glaucoma screening from fundus image,” *IEEE Transactions on Medical Imaging*, vol. 37, no. 11, pp. 2493–2501, 2018.
- [14] X. Hu *et al.*, “Glim-net: Chronic glaucoma forecast transformer for irregularly sampled sequential fundus images,” *IEEE Transactions on Medical Imaging*, vol. 42, no. 6, pp. 1875–1884, 2023.
- [15] Y. Zhou, L. Huang, T. Zhou, and L. Shao, “Cct-net: Category-invariant cross-domain transfer for medical single-to-multiple disease diagnosis,” in *2021 IEEE/CVF International Conference on Computer Vision (ICCV)*, 2021, pp. 8240–8250.
- [16] H. Wang *et al.*, “A workflow for computer-aided diagnosis of glaucoma,” in *2022 IEEE International Symposium on Biomedical Imaging Challenges (ISBIC)*, 2022, pp. 1–4.
- [17] D. Das, D. R. Nayak, and R. B. Pachori, “Glaucoformer: Dual-domain global transformer network for generalized glaucoma stage classification,” *IEEE Journal of Biomedical and Health Informatics*, vol. 29, no. 11, pp. 8450–8459, 2025.
- [18] D. Das and D. R. Nayak, “Fja-net: A fuzzy joint attention guided network for classification of glaucoma stages,” *IEEE Transactions on Fuzzy Systems*, vol. 32, no. 10, pp. 5438–5448, 2024.
- [19] S. Asrani, L. Essaid, B. D. Alder, and C. Santiago-Turla, “Artifacts in spectral-domain optical coherence tomography measurements in glaucoma,” *JAMA Ophthalmology*, vol. 132, no. 4, pp. 396–402, 04 2014.
- [20] T. Heikka and N. M. Jansonius, “Influence of signal-to-noise ratio, glaucoma stage and segmentation algorithm on oct usability for quantifying layer thicknesses in the peripapillary retina,” *Acta Ophthalmologica*, vol. 101, no. 3, pp. 251–260, 2023.
- [21] R. Malik, W. H. Swanson, and D. F. Garway-Heath, “‘structure–function relationship’ in glaucoma: past thinking and current concepts,” *Clinical & Experimental Ophthalmology*, vol. 40, no. 4, pp. 369–380, 2012.
- [22] C. Bowd *et al.*, “Bayesian machine learning classifiers for combining structural and functional measurements to classify healthy and glaucomatous eyes,” *Investigative ophthalmology & visual science*, vol. 49 3, pp. 945–53, 2008.
- [23] A. Anton *et al.*, “Diagnostic accuracy and detection rate of glaucoma screening with optic disk photos, optical coherence tomography images, and telemedicine,” *Journal of Clinical Medicine*, vol. 11, no. 1, 2022.
- [24] J. Wu, H. Fang, F. Li *et al.*, “Gamma challenge: Glaucoma grading from multi-modality images,” *Medical Image Analysis*, vol. 90, p. 102938, 2023.
- [25] W. Li and C.-M. Pun, “Elf: An end-to-end local and global multimodal fusion framework for glaucoma grading,” in *2023 IEEE International Conference on Bioinformatics and Biomedicine (BIBM)*, 2023, pp. 4081–4085.
- [26] Z. Wang *et al.*, “Mstnet: method for glaucoma grading based on multimodal feature fusion of spatial relations,” *Physics in Medicine & Biology*, vol. 68, no. 24, p. 245002, dec 2023.
- [27] Z. Cai, L. Lin, H. He, and X. Tang, “Corolla: An efficient multi-modality fusion framework with supervised contrastive learning for glaucoma grading,” in *2022 IEEE 19th International Symposium on Biomedical Imaging (ISBI)*, 2022, pp. 1–4.
- [28] Y. Wang *et al.*, “Geometric correspondence-based multimodal learning for ophthalmic image analysis,” *IEEE Transactions on Medical Imaging*, vol. 43, no. 5, pp. 1945–1957, 2024.
- [29] Z. Yang *et al.*, “Etscl: An evidence theory-based supervised contrastive learning framework for multi-modal glaucoma grading,” in *Ophthalmic Medical Image Analysis (OMIA) at MICCAI*, 2024, pp. 11–21.
- [30] H. Raja *et al.*, “Data on oct and fundus images for the detection of glaucoma,” *Data in Brief*, vol. 29, p. 105342, 2020.
- [31] X. Huang *et al.*, “Grape: A multi-modal dataset of longitudinal follow-up visual field and fundus images for glaucoma management,” *Scientific Data*, vol. 10, no. 1, p. 520, 2023.
- [32] Y. Luo *et al.*, “Harvard glaucoma fairness: A retinal nerve disease dataset for fairness learning and fair identity normalization,” *IEEE Transactions on Medical Imaging*, vol. 43, no. 7, pp. 2623–2633, 2024.
- [33] F. A. Medeiros *et al.*, “Estimating the rate of retinal ganglion cell loss in glaucoma,” *American Journal of Ophthalmology*, vol. 154, no. 5, pp. 814–824.e1, 2012.
- [34] A. Bayer, *Combining Structure and Function in Glaucoma*. Cham: Springer International Publishing, 2018, pp. 329–343.
- [35] Z. Chen *et al.*, “Combination of enhanced depth imaging optical coherence tomography and fundus images for glaucoma screening,” *Journal of medical systems*, vol. 43, no. 6, p. 163, 2019.
- [36] T. Watanabe *et al.*, “Combining optical coherence tomography and fundus photography to improve glaucoma screening,” *Diagnostics*, vol. 12, no. 5, 2022.
- [37] A. Kamalipour *et al.*, “Combining optical coherence tomography and optical coherence tomography angiography longitudinal data for the detection of visual field progression in glaucoma,” *American Journal of Ophthalmology*, vol. 246, pp. 141–154, 2023.
- [38] E. E. Hwang *et al.*, “Utilization of image-based deep learning in multimodal glaucoma detection neural network from a primary patient cohort,” *Ophthalmology Science*, vol. 5, no. 3, p. 100703, 2025.
- [39] Y. Li, Y. Han, Z. Li, Y. Zhong, and Z. Guo, “A transfer learning-based multimodal neural network combining metadata and multiple medical images for glaucoma type diagnosis,” *Scientific Reports*, vol. 13, 2023.
- [40] M.-I. Georgescu *et al.*, “Multimodal multi-head convolutional attention with various kernel sizes for medical image super-resolution,” in *2023 IEEE/CVF Winter Conference on Applications of Computer Vision (WACV)*, 2023, pp. 2194–2204.
- [41] J. Dhar *et al.*, “Multimodal fusion learning with dual attention for medical imaging,” in *2025 IEEE/CVF Winter Conference on Applications of Computer Vision (WACV)*, 2025, pp. 4362–4371.

- [42] P. Khosla *et al.*, "Supervised contrastive learning," in *Advances in Neural Information Processing Systems*, H. Larochelle, M. Ranzato, R. Hadsell, M. Balcan, and H. Lin, Eds., vol. 33. Curran Associates, Inc., 2020, pp. 18 661–18 673.
- [43] K. He *et al.*, "Masked autoencoders are scalable vision learners," in *Proceedings of the IEEE/CVF Conference on Computer Vision and Pattern Recognition (CVPR)*, June 2022, pp. 16 000–16 009.
- [44] D. Shi *et al.*, "A multimodal visual–language foundation model for computational ophthalmology," *npj Digital Medicine*, 2025.
- [45] R. Bachmann, D. Mizrahi, A. Atanov, and A. Zamir, "Multimae: Multimodal multi-task masked autoencoders," in *European Conference on Computer Vision (ECCV)*, 2022, pp. 348–367.
- [46] K. Yu *et al.*, "Urfound: Towards universal retinal foundation models via knowledge-guided masked modeling," in *Medical Image Computing and Computer Assisted Intervention – MICCAI 2024*, 2024, pp. 753–762.
- [47] K. Tian *et al.*, "Designing bert for convolutional networks: Sparse and hierarchical masked modeling," in *In Proceedings of the International Conference on Learning Representations (ICLR)*, 2023.
- [48] S. Ogawa *et al.*, "Association between combined structure function index and glaucoma severity," *Journal of Ophthalmology*, vol. 2019, no. 1, p. 9414675, 2019.
- [49] L. Li *et al.*, "A large-scale database and a cnn model for attention-based glaucoma detection," *IEEE Transactions on Medical Imaging*, vol. 39, no. 2, pp. 413–424, 2020.
- [50] K. He, X. Zhang, S. Ren, and J. Sun, "Deep residual learning for image recognition," in *2016 IEEE Conference on Computer Vision and Pattern Recognition (CVPR)*, 2016, pp. 770–778.
- [51] F. Chollet, "Xception: Deep learning with depthwise separable convolutions," in *2017 IEEE Conference on Computer Vision and Pattern Recognition (CVPR)*, 2017, pp. 1800–1807.
- [52] C. Zhang, Z. Yang, X. He, and L. Deng, "Multimodal intelligence: Representation learning, information fusion, and applications," *IEEE Journal of Selected Topics in Signal Processing*, vol. 14, no. 3, pp. 478–493, 2020.
- [53] C. Guo, G. Pleiss, Y. Sun, and K. Q. Weinberger, "On calibration of modern neural networks," in *Proceedings of the 34th International Conference on Machine Learning - Volume 70*, ser. ICML'17. JMLR.org, 2017, p. 1321–1330.
- [54] A. Dosovitskiy *et al.*, "An image is worth 16x16 words: Transformers for image recognition at scale," in *In Proceedings of the International Conference on Learning Representations (ICLR)*, 2021.
- [55] Z. Liu *et al.*, "A convnet for the 2020s," *Proceedings of the IEEE/CVF Conference on Computer Vision and Pattern Recognition (CVPR)*, 2022.
- [56] R. R. Selvaraju *et al.*, "Grad-cam: Visual explanations from deep networks via gradient-based localization," in *2017 IEEE International Conference on Computer Vision (ICCV)*, 2017, pp. 618–626.
- [57] S. Woo, J. Park, J.-Y. Lee, and I. S. Kweon, "Cbam: Convolutional block attention module," in *Proceedings of the European Conference on Computer Vision (ECCV)*, September 2018.